Radiopharmaceutical imaging based on 3D-CZT Compton camera with 3D-printed mouse phantom

Feng Tian [a], Changran Geng [a,*], Zhiyang Yao [b], Renyao Wu [a], Jianfeng Xu [a,c], Fei Cai [a,c], Xiaobin Tang [a]

[a] *Department of Nuclear Science and Technology, Nanjing University of Aeronautics and Astronautics, Nanjing 210016, People's Republic of China*
[b] *Department of Engineering Physics, Tsinghua University, Beijing 100084, People's Republic of China*
[c] *JYAMS PET Research and Development Limited, Nanjing 211100, People's Republic of China*

ARTICLE INFO

ABSTRACT

Purpose: The study proposes the use of three-dimensional CdZnTe Compton camera (3D-CZT CC) for radiopharmaceutical imaging and investigates the influence factors using a 3D-printed mouse phantom.
Methods: The event selection method and image reconstruction algorithm are optimized by Monte Carlo simulations and mouse phantom experiments.
Results: Simulation results show that the intrinsic energy resolution and spatial resolution of 3D-CZT cause a certain deviation in the calculated Compton scattering angle and Compton axis. Such deviation causes the imaging quality to deteriorate. By selecting events whose distance between Compton and photoelectronic interactions are larger than 10 mm, the mean deviation of the Compton axis could be reduced to less than 10%. Using the ordered origin ensemble algorithm with resolution recovery, the artifacts around organs where the radiopharmaceutical was placed are reduced, and the quality of the reconstruction results are improved compared to the results with simple back projection and origin ensembles algorithms. The phantom study shows that the 3D-CZT CC imaging device could visualize the radiopharmaceuticals distribution by 15 min detection.
Conclusions: Through the analysis of this study, the feasibility of 3D-CZT CC for *in-vivo* distribution measurement of radiopharmaceuticals is demonstrated, and the quality of reconstruction result has been improved.

1. Introduction

Radiopharmaceuticals are drugs labeled with specific nuclides, and they have been widely used in functional imaging and cancer treatment [1,2]. Radiopharmaceutical imaging can offer accurate diagnoses, enhanced visualization, and effective individual treatments for a range of diseases [1,3]. At present, positron emission tomography (PET) and single-photon emission computed tomography (SPECT) are the most commonly used medical imaging techniques for nuclear medicine [4]. With the development of medical imaging technology, higher requirements are put forward for imaging devices, such as the wide detectable energy range, excellent energy resolution and spatial resolution, et al [5]. In contrast, PET can only measure 511 keV gamma rays, whereas SPECT usually detect the gamma ray emitting tracers with energy less than ~300 keV [6]. In addition, SPECT cannot achieve high detection efficiency due to the mechanical collimator [7]. To address the limitation of the energy of gamma rays and realize high detection

efficiency and high spatial resolution, Compton Camera (CC) based on electronic collimation was proposed for medical imaging [8,9].

CC has been extensively studied in terms of theoretical feasibility analysis and equipment optimization [10–12]. According to the structure of the detector, CCs are divided into two main categories, i.e., multilayer CC and single-layer CC [13–15]. Multilayer CCs have been widely studied, and a large number of related clinical medical imaging experiments have been carried out. S. Liprandi et al developed a CC prototype for ion beam range monitoring which consists of a stack of 6 double-side silicon strip detectors as scatter component and a large monolithic $LaBr_3(Ce)$ scintillation crystal as absorber components [16]. M. Sakai developed a medical imaging technique using a CC, which consisted of one layer of Si detector and three layers of cadmium telluride detectors [17]. In contrast, $Cd_{0.9}Zn_{0.1}Te$ (CZT, density is 5.8 g/cm^3) is a kind of semiconductor which can be used at room temperature, so the detectors based on CZT have attracted extensive attention. Some CCs based CZT have also been developed and applied to medical
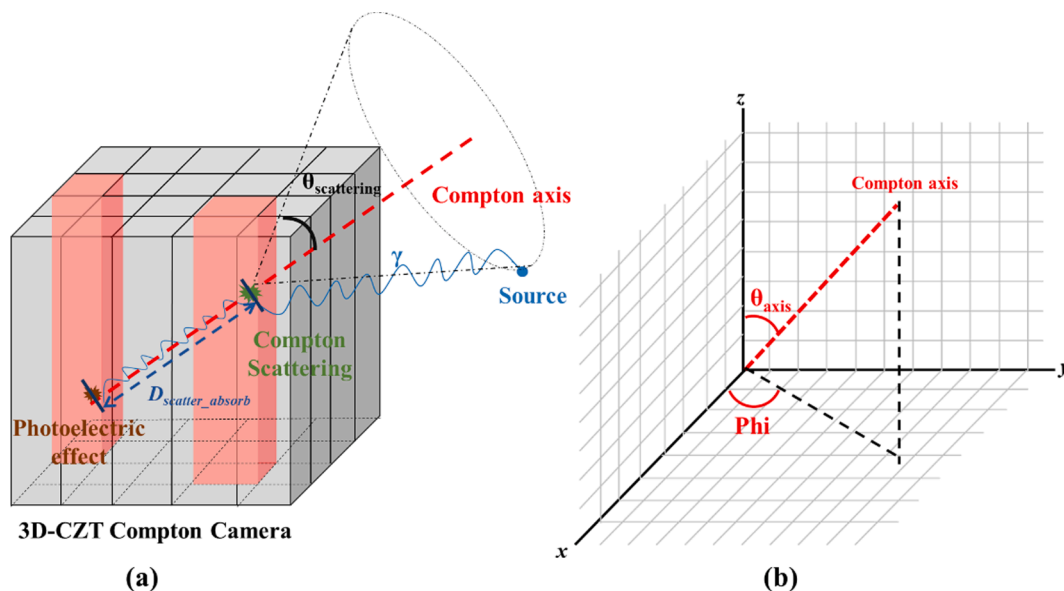
Fig. 1. Principle of 3D-CZT CC. (a) Schematic of the true event of the 3D-CZT Compton camera. $\theta_{scattering}$ is the Compton scattering angle. The red dotted line is the Compton axis. The blue dotted line is $D_{scatter\_absorb}$. (b) Theta and Phi angles of Compton axis in spherical coordinate system. (For interpretation of the references to colour in this figure legend, the reader is referred to the web version of this article.)

imaging research. C. Golnik et al developed a Compton imaging prototype to monitor proton range which consists of a CZT cross strip detector as a scatter plane and three BGO block detector as absorber plane [18]. With the development of crystal growth technology and circuit readout technology in recent years, the three-dimensional coordinates of the photon interactions in a single CZT crystal can be obtained. Thus, a single CZT crystal can be used as a single-layer CC with the depth of interaction (DOI) technique [19]. Relative to multilayer CCs, the three-dimensional CZT (3D-CZT) CC has the advantages of large field of view, high energy resolution and spatial resolution [20,21]. Some groups have successfully developed such devices [19,22]. E. Draeger et al used an equipment consisted of four separate 3D-CZT CC to monitor the proton range through detecting the distribution of prompt gammas emitted during the irradiation [23].

Although the 3D-CZT CC shows great performances, no study has explored its use in radiopharmaceutical imaging. Therefore, this work proposes the use of the single-layer 3D-CZT CC in radiopharmaceutical imaging. The event selection method based on event distance is proposed to reduce the deviation of the Compton scattering angle and Compton axis. In the aspect of reconstruction algorithm optimization, the ordered origin ensemble algorithm with resolution recovery (OE-RR) is used to eliminate artifacts in reconstruction images. The performance of this imaging device in medical imaging is then evaluated by conducting radiopharmaceutical measurement experiments on the basis of a mouse phantom.

2. Materials and methods

2.1. Compton camera and image reconstruction algorithm

The CC reconstructs the origin of gamma sources by employing Compton kinematics. When an incident gamma ray causes a Compton scattering reaction in the detector, the scattered photon can be further absorbed by the photoelectric effect [24]. The Compton scattering angle can be calculated by combining the positions and energy deposition of the two reactions (i.e., Compton scattering and photoelectric event), as shown in Equation (1):.

$$cos\theta = 1 - \frac{m_e c^2 E_1}{E_2(E_1 + E_2)} \tag{1}$$

where E_1 is the energy deposited in the Compton scattering, E_2 is the energy deposited in the photoelectric effect, and $m_e c^2$ is the rest mass energy of an electron.

The principle of the 3D-CZT CC is shown in Fig. 1(a). The Compton axis is the connecting line between the position of a scattering event (i. e., Compton interaction) and an absorbing event (i.e., photoelectronic interaction). The three-dimensional spatial position of the Compton axis can be represented by a theta angle (θ_{axis}) and phi angle (*Phi*) in the spherical coordinate system, as shown in Fig. 1(b). We define $D_{scatter\_absorb}$ as the distance between the positions of a scattering event and an absorbing event.

To reconstruct the radiopharmaceutical distribution, we use three types of algorithms, i.e., simple back projection (SBP), origin ensemble (OE) and ordered OE-RR. SBP is the simplest and fastest algorithm to obtain the distribution of radioactive sources, but it generates many artifacts in the reconstruction images. The process of OE iterative reconstruction is equivalent to the Markov Chain Monte Carlo sampling of the probability distributions of origin locations corresponding to the acquired data [25]. OE-RR algorithm obtained the representative points on the "guess" cones determined by randomly corrected data corresponding to the measured data, which samples from the distributions of the positions of interactions in projection elements and deposited energies [26]. Recently, an ordered OE-RR was proposed to accelerate the speed of OE iteration with resolution recovery [27]. In this study, we use the ordered OE-RR to recover the degraded images caused by the finite spatial and energy resolution of the CC prototype and thereby obtain better reconstruction. The number of iterations for reconstruction of all results is 10000. The size of imaging plane is 10×10 cm^2. Considering the size of the mouse, the imaging plane is selected to be 8.5–11.5 cm from the detector surface whereas the center of the imaging plane is 10 cm from the detector surface.

2.2. 3D-CZT Compton camera

In this study, the CZT camera prototype is developed by the Kromek group. The size of the CZT crystal is $22 \times 22 \times 15$ mm^3. This CC is fabricated with a common planar cathode and 11×11 pixelated anode pads. The detector is operated with the cathode biased at -3000 V. An HPL v1.3 application-specific integrated circuit (ASIC) readout system is used to measure the waveform signals and trigger signals of all channels
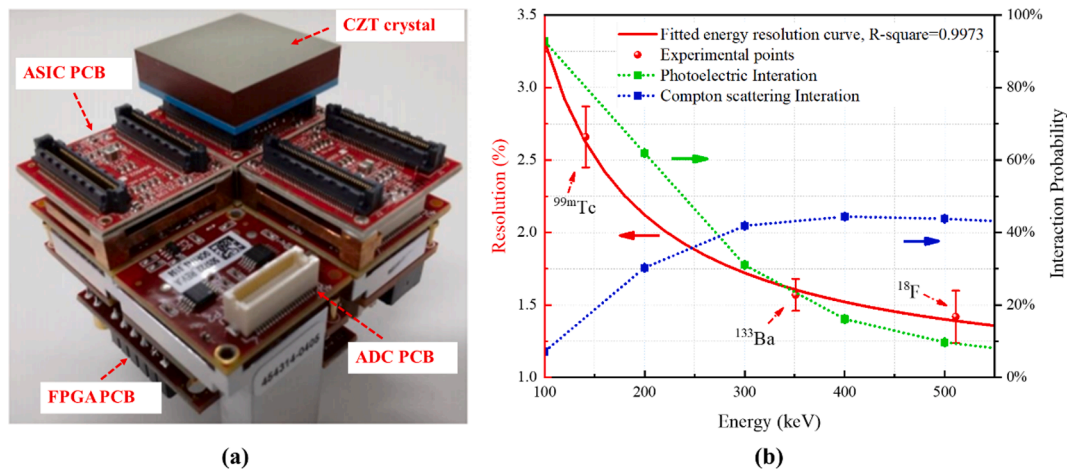
Fig. 2. Properties of the 3D-CZT camera. (a) Structure of 3D-CZT camera, (b) Energy resolution of this 3D-CZT detector which is the value of FWHM to the energy of incident gamma ray.
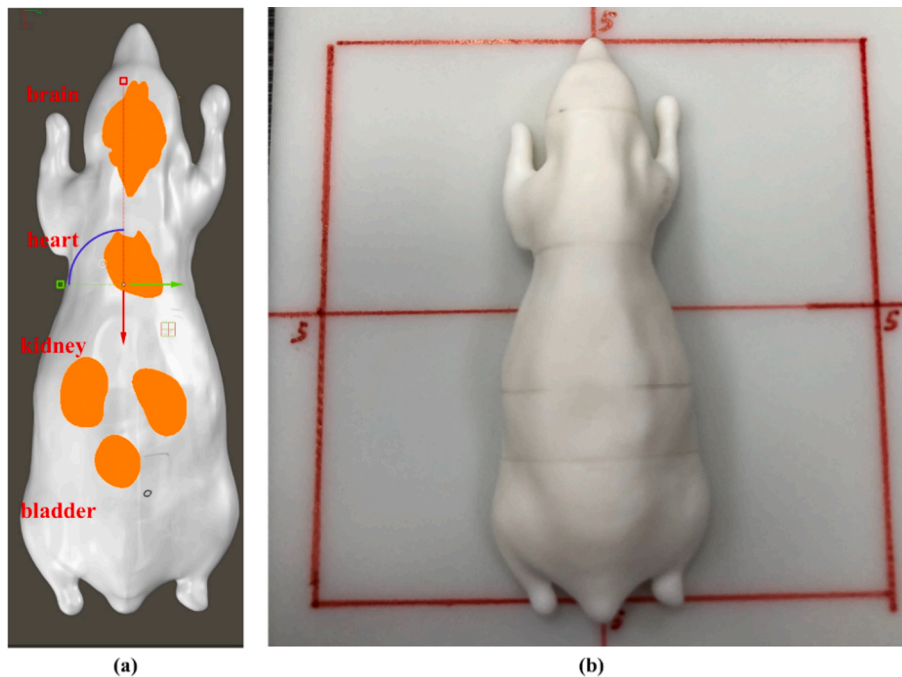

Fig. 3. Mouse phantom used in this study. (a) Structure diagram, (b) 3D-printed mouse phantom.

[28]. The outputs are $14 - $ bit sample data which are written as list mode data, and the amplitude and timing information are acquired simultaneously by using two signal processing paths at each channel. The timing of the anode and cathode signals can be accurately measured through the peak detector's circuit in ASIC [29]. The time-to-digital-converter's signal is converted into digital signal by analog-to-digital converter, and then transmitted through a field-programmable gate array. The time resolution of this 3D-CZT CC is about 25 ns and the dead time of each event is about 250 ns. The pile up probability of this 3D-CZT CC is about 20% when the count rate is 220 kcps. The structure of the 3D-CZT is shown in Fig. 2(a). The interaction depth is inferred by calculating the electron cloud drift time on the basis of the time difference between the signals of the cathode and the anode so that the three-dimensional coordinates of Compton events can be obtained [19]. The angular resolution measure (ARM) of this 3D-CZT CC is $15.90 \pm 0.33°$ obtained in the previous Monte Carlo simulations. The energy resolution (*R*) of the 3D-CZT CC under different energies is fitted through

experimental results. The fitting formula is shown in Eq. (2), and the fitting result is shown in Fig. 2b.

$$R = \frac{a + b\sqrt{E + cE^2}}{E} \qquad (2)$$

2.3. 3D-printed mouse phantom

A 3D-printed mouse phantom is used to analyze the performance of the 3D-CZT CC in radiopharmaceutical distribution imaging as shown in Fig. 3. The phantom is generated using a co-registered CT and the cryosection images of a 28 g nude normal male mouse, resulting in a matrix size of $380 \times 992 \times 208$ and 0.1 mm cubical voxels [30]. Butanediol dimethacrylate ($C_{12}H_{18}O_4$, ρ: 1.3 g/cm^3) is selected as the 3D-printed material. To facilitate the placement of the radiopharmaceutical, we divide the phantom into five parts, and the brain, heart, kidney, and bladder areas are hollowed out. The organs analyzed in this study are the brain and bladder.
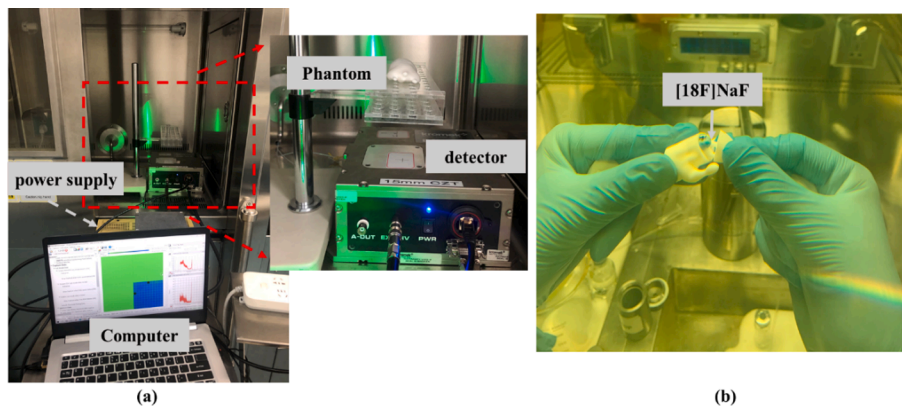
Fig. 4. Experimental setup. (a) Instrument used in the experiment. (b) Schematic of radiopharmaceutical placement.
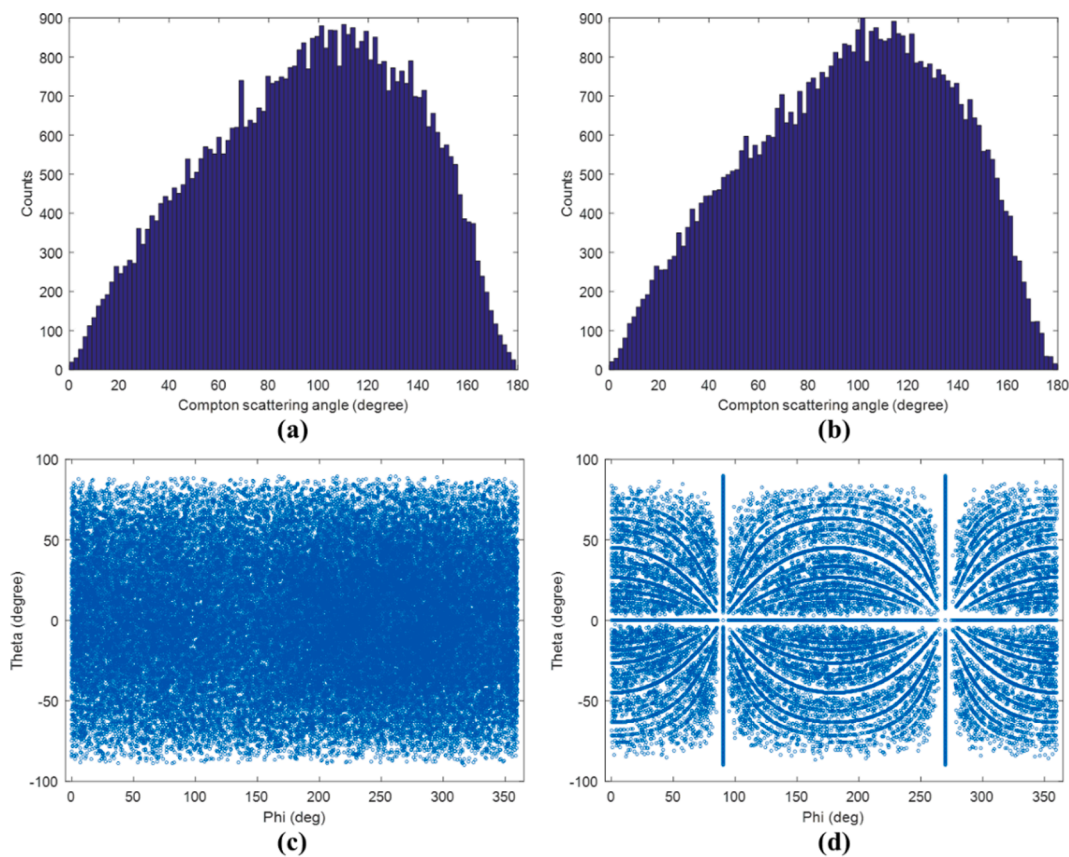

Fig. 5. Analysis of the physical properties of the 3D-CZT. (a) Compton scattering angle distribution without consideration of the energy resolution of the 3D-CZT; (b) Compton scattering angle distribution with consideration of the energy resolution of the 3D-CZT; (c) Compton axis distribution without consideration of the spatial resolution of the 3D-CZT; (d) Compton axis distribution with consideration of the spatial resolution of 3D-CZT.

2.4. Monte Carlo toolkit and configuration

The Monte Carlo toolkit Geant4 (version 10.05) with QGSP_BIC physics list is used to simulate the radiation transportation. The geometry of the Monte Carlo simulation is based on the subsequent experimental settings. The material of the torso is $C_{12}H_{18}O_4$, and the material of the organ is water in which the radiopharmaceutical is placed. In simulations, the number of gamma ray with 511 keV emitted from brain and bladder are 4.662×10^8 and 2.331×10^8, respectively. A 64-bit Linux computer with Intel Xeon(R) CPU E5-2699 v4 is used to run the Geant4 codes and ordered OE-RR algorithm.

2.5. Experimental conditions

The purpose of this study is to analyze the performance of the 3D-CZT CC used in radiopharmaceutical imaging. For the experiments, [18F]sodium fluoride ([18F]NaF) provided by JYAMS PET Research and Development Limited is selected. During the experiment, [18F]NaF solution is placed in a sealed capsule located in the brain and bladder with ~14 and ~7 μCi, respectively. The material of the capsule is mainly gelatin, and the thickness is about 0.110 ± 0.015 mm. Because the size of the capsule is very small, it would not affect the transport process of gamma ray with 511 keV. Therefore, in the Monte Carlo simulations, capsule has not been considered. The phantom is placed ~10 cm above the detector, and the center of the CZT crystal is basically aligned with
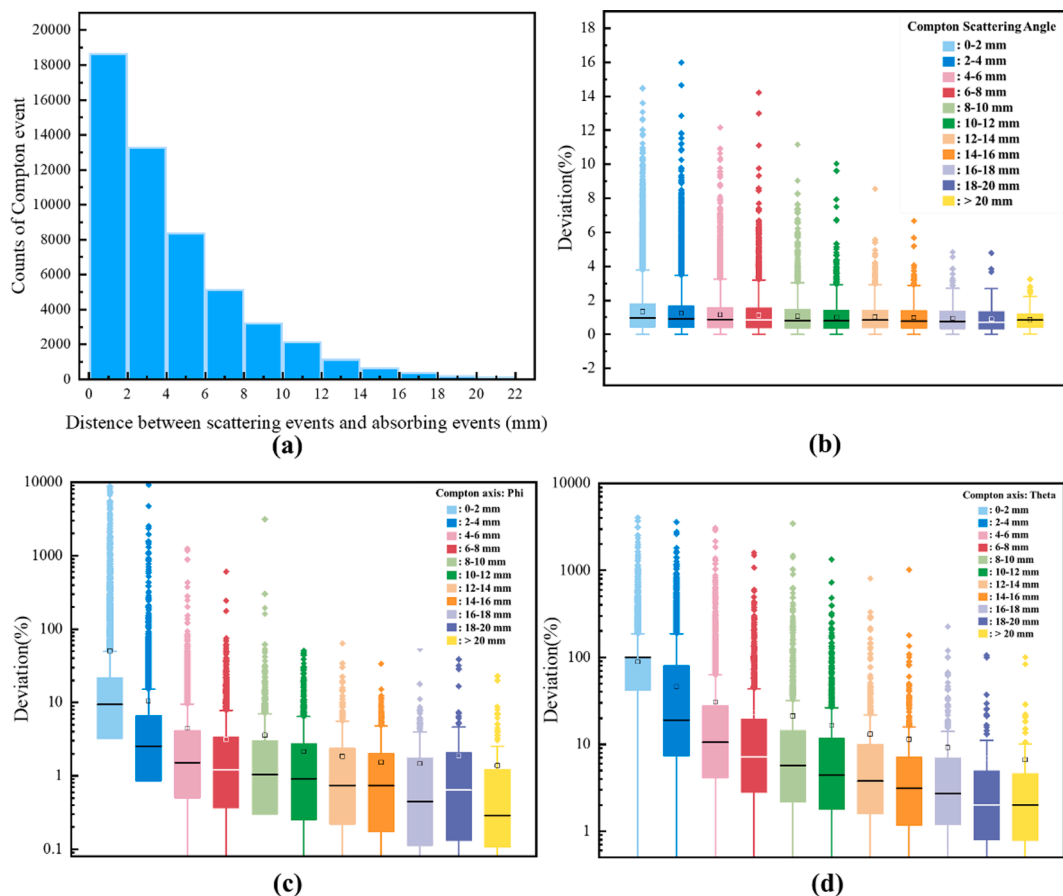
Fig. 6. Influence of event distance on Compton data. (a) Relationship between the counts of Compton events and distance between the scattering event and the absorbing event; (b) deviation of Compton scattering angle at different $D_{scatter\_absorb}$; (c) deviation of phi angle of Compton axis at different $D_{scatter\_absorb}$; (d) deviation of theta angle of Compton axis at different $D_{scatter\_absorb}$.

the phantom center. The radiopharmaceuticals are set in the brain and bladder separately or simultaneously. Each group of experiments is measured for 1 h, and the detection data are collected every 15 min. The experimental setup is shown in Fig. 4.

3. Results

3.1. Influence of energy resolution and spatial resolution

The Monte Carlo simulation is used to analyze the deviations in the Compton data (i.e., Compton scattering angle and Compton axis) caused by the energy and spatial resolutions. In the simulations, the radiopharmaceuticals are located simultaneously in the brain and bladder with activities of 14 and 7 μCi, respectively. The reaction position and deposition energy of the particles are directly recorded without considering the energy and spatial resolutions in the Monte Carlo simulations. Then, the influence of these resolutions on the Compton data are considered in the data postprocessing. The energy window is set to 501–521 keV for selecting effective Compton events. The Compton scattering angle is calculated with Eq. (1). Fig. 5(a) shows the Compton scattering angle distribution without consideration of the energy resolution. Fig. 5(b) presents the Compton scattering angle distribution with consideration of the energy resolution. Comparing the two results shows that the Compton scattering angle distribution is basically the same regardless of the consideration of energy resolution. Fig. 5(c) shows the spatial distribution of the Compton axis in the spherical coordinate system without consideration of the spatial resolution. Fig. 5(d) presents the spatial distribution of the Compton axis with consideration of the spatial resolution. A clear difference is noted between the two results.

Specifically, the exact Compton axis distribution is basically uniform, while considering the spatial resolution, the distribution of the Compton axis shows "eyelid" bands. The concentric "eyelid" bands arise from the pixelation of the 3D-CZT CC [22].

Some studies have shown that the deviation of the Compton axis is mainly affected by the intrinsic spatial resolution of the CC and $D_{scatter\_absorb}$ [31]. Therefore, we analyze the relationship between the $D_{scatter\_absorb}$ and the deviation of the Compton axis in this section. Fig. 6(a) is the number of effective Compton events at different $D_{scatter\_absorb}$. When $D_{scatter\_absorb}$ increases, the counts of effective Compton events at the corresponding distance decreases. Fig. 6(b) shows the absolute value of the relative deviation of the Compton scattering angle at different $D_{scatter\_absorb}$ when the energy resolution is considered. And the mean and median values of the Compton scattering angle deviation are almost fixed for different $D_{scatter\_absorb}$, thereby indicating that the $D_{scatter\_absorb}$ would not affect the deviation of the Compton scattering angle. This result is mainly due to the Compton scattering angle being related to the energy resolution only but being independent of the spatial resolution. Fig. 6(c and d) are the deviations of the Compton axis at different $D_{scatter\_absorb}$ with consideration of the spatial resolution. For the phi and theta angles of the Compton axis in the spherical coordinate system, the influence of $D_{scatter\_absorb}$ on deviation show the same trend, that is, the greater the $D_{scatter\_absorb}$ is, the smaller the deviation is. At the same $D_{scatter\_absorb}$, the deviation of the theta angle is larger than that of the phi angle. However, the count of effective Compton events in each distance segment is considerably small when the distance is greater than 10 mm, and the reduction of deviations is not significant. To ensure the accuracy of the reconstruction images, a sufficient count of effective Compton events is needed. Therefore, the minimum distance between the
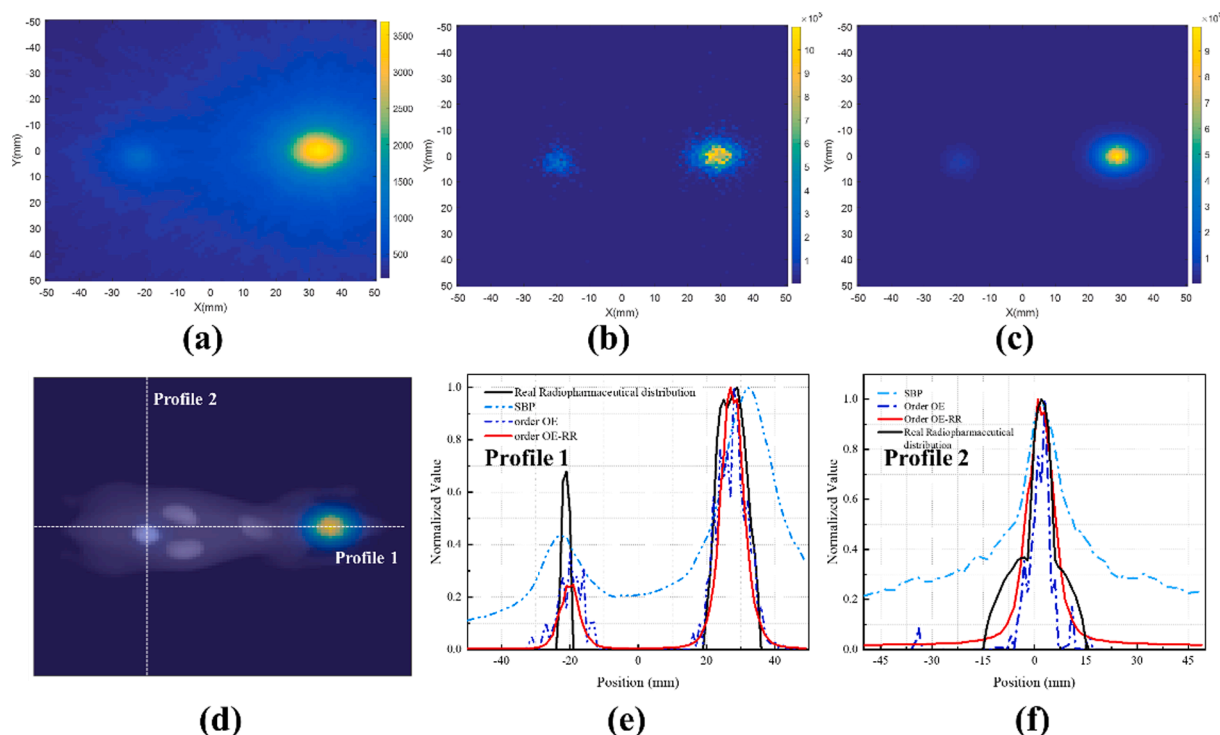
Fig. 7. Compton reconstruction results based on simulated data. (a) Reconstruction result of the SBP algorithm; (b) Reconstruction result of the OE algorithm; (c) Reconstruction result of the ordered OE-RR algorithm; (d) Result of the fusion of the reconstruction result of the ordered OE-RR algorithm with the actual placement map of the mouse phantom in the simulations; (e) Radiopharmaceutical distribution reconstructed by different algorithm as shown in dashed line 1 of (d); (f) Radiopharmaceutical distribution reconstructed by different algorithm as shown in dashed line 2 of (d).

Compton and photoelectronic interactions selected in this study is 10 mm.

3.2. Comparison of image qualities with different reconstruction algorithms

Fig. 7(a) shows the result of the SBP with consideration of the energy and spatial resolutions. Although the SBP result clearly distinguished the two organs, there are a lot of artifacts. Fig. 7(b) shows the OE result. Although the artifacts around the organs are reduced relative to the SBP result, the accurate distribution of the radiopharmaceuticals could not be obtained in the OE result. Fig. 7(c) shows the result obtained by the ordered OE-RR algorithm. The spatial distribution of the

radiopharmaceuticals in the organs is reconstructed, and the artifacts are fewer than those in the results of the SBP or OE. Fig. 7(d) shows the fusion of the ordered OE-RR result and the mouse phantom. It can be seen that the result obtained by ordered OE-RR can achieve the accurate radiopharmaceuticals imaging in mouse organs set in the simulations. Fig. 7(e and f) show the plot profiles of the Fig. 7(d) at the plane indicated by the white dotted lines. It can be seen that the radiopharmaceutical distribution reconstructed by order OE-RR algorithms is the most consistent with the radiopharmaceutical distribution set in simulations.

In addition, the contrast (V_{con}) is used as a parameter for quantitative analysis of image quality. The calculation formula of V_{con} is shown in Eq. (3):.
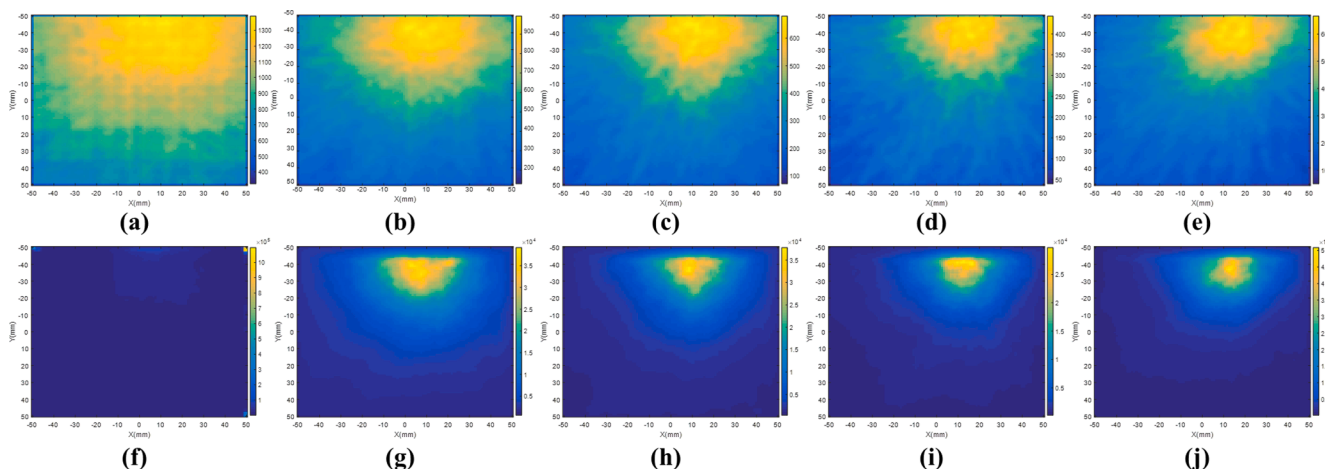

Fig. 8. Reconstruction results in the case of radiopharmaceuticals placed in the brain. (a)–(e) SBP results when $D_{scatter\_absorb}$ are 2–4, 4–6, 6–8, 8–10, and over 10 mm. (f)–(j) Ordered OE-RR results when $D_{scatter\_absorb}$ are 2–4, 4–6, 6–8, 8–10, and over 10 mm, respectively.
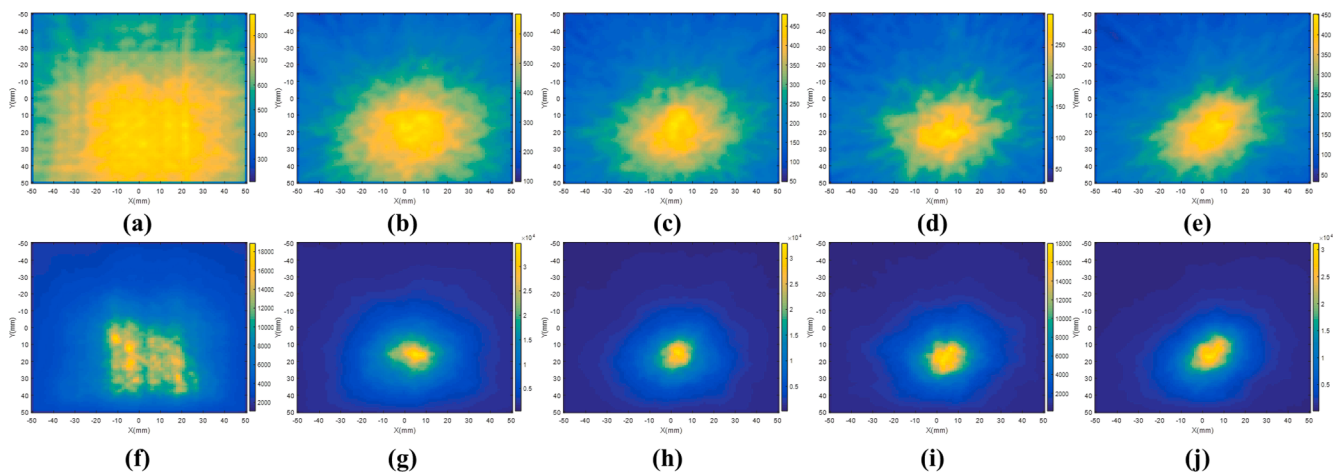
Fig. 9. Reconstruction results in the case of the radiopharmaceuticals placed in the bladder. (a)–(e) SBP results when $D_{scatter\_absorb}$ are 2–4, 4–6, 6–8, 8–10, and over 10 mm. (f)–(j) Ordered OE-RR results when $D_{scatter\_absorb}$ are 2–4, 4–6, 6–8, 8–10, and over 10 mm.

Fig. 10. Reconstruction results in the case of the radiopharmaceuticals placed in the brain and bladder. (a)–(e) SBP results when $D_{scatter\_absorb}$ are 2–4, 4–6, 6–8, 8–10, and over 10 mm. (f)–(j) ordered OE-RR results when $D_{scatter\_absorb}$ are 2–4, 4–6, 6–8, 8–10, and over 10 mm.
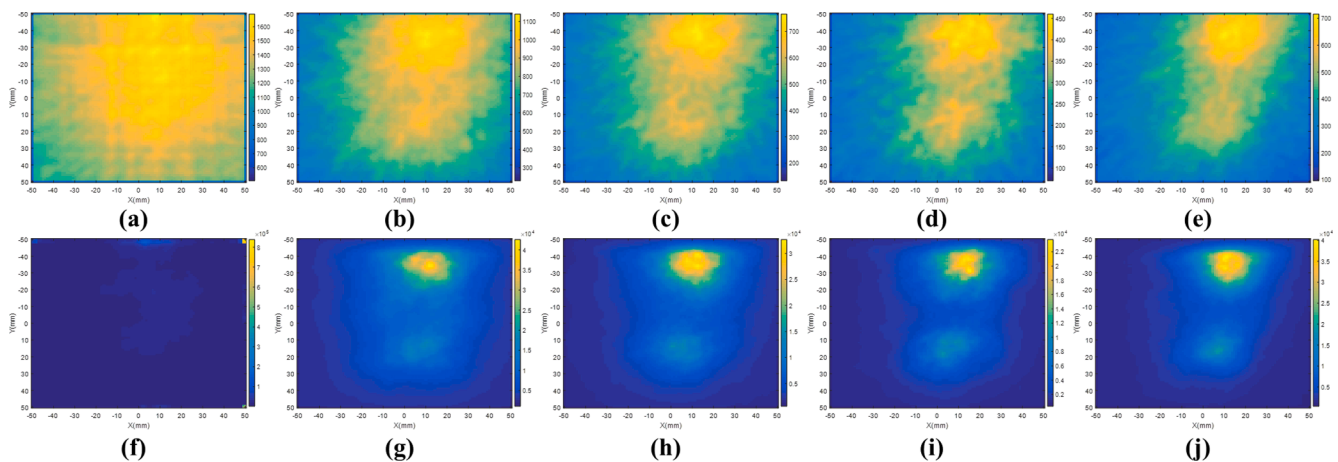
$$V_{con} = \frac{N_{ROI}}{N_{Background}} \tag{3}$$

where N_{ROI} is the sum of pixel values in ROI and $N_{Background}$ is the sum of pixel values in all regions of mouse phantom except ROI. In this study, ROI is defined as the brain and bladder of mouse phantom. The V_{con} of SBP is only 0.19. In contrast, when order OE iterative algorithm is used, V_{con} can be improved to 1.04. Furthermore, when using the order OE-RR algorithm, the V_{con} can be improved to 1.45.

3.3. Reconstructed images based on experimental data

In this section, experiments are conducted to further evaluate the actual imaging performance of 3D-CZT CC. The experiments mainly analyzed the relationship between the reconstruction results and the detection times in the presence of radiopharmaceuticals in the brain and bladder separately or simultaneously. For the experimental data, the scattering and absorbing events are judged by their energy depositions, i.e., the scattering event generally has greater energy deposition than the absorbing event [32]. Figs. 8 and 9 show the reconstruction results of the Compton data measured under 1 h of data collection when the radiopharmaceuticals are placed in the brain or bladder separately. Fig. 10 show the results when the radiopharmaceuticals are placed in the brain and bladder simultaneously. Fig. 8(a–e) are the results with the SBP algorithm for the scattering and absorbing events with $D_{scatter\_absorb}$ of

2–4, 4–6, 6–8, 8–10, and over 10 mm. Fig. 8(f–j) show the results with the ordered OE-RR algorithm under the different distances of effective Compton events. These results prove that the greater the $D_{scatter\_absorb}$ is, the higher the quality of the reconstructed images obtained by the SBP and the ordered OE-RR algorithm is. The artifacts in the ordered OE-RR results are significantly fewer than those in the SBP results. For the other imaging sites, the results are similar, as shown in Figs. 9–10. Regardless of the number of organs with radiopharmaceuticals, the distribution of the radiopharmaceuticals can be identified clearly in the reconstruction results.

The relationship between detection time and imaging quality is explored. Fig. 11(a–d) show the reconstruction results of the ordered OE-RR algorithm under the detection times of 15, 30, 45, and 60 min. Fig. 11(e) shows the reconstruction result of the 15 min detection superimposed with the mouse phantom set in the experiments. It can be seen that the distribution of the radiopharmaceuticals in the organs is visualized in the 15 min detection when the activities of the radiopharmaceuticals in the organs are at the clinical level. Within 15 min detection time, the count of effective Compton event is about 4200, and the reconstruction time is only about 10 s with the Intel Xeon(R) CPU E5-2699 v4.
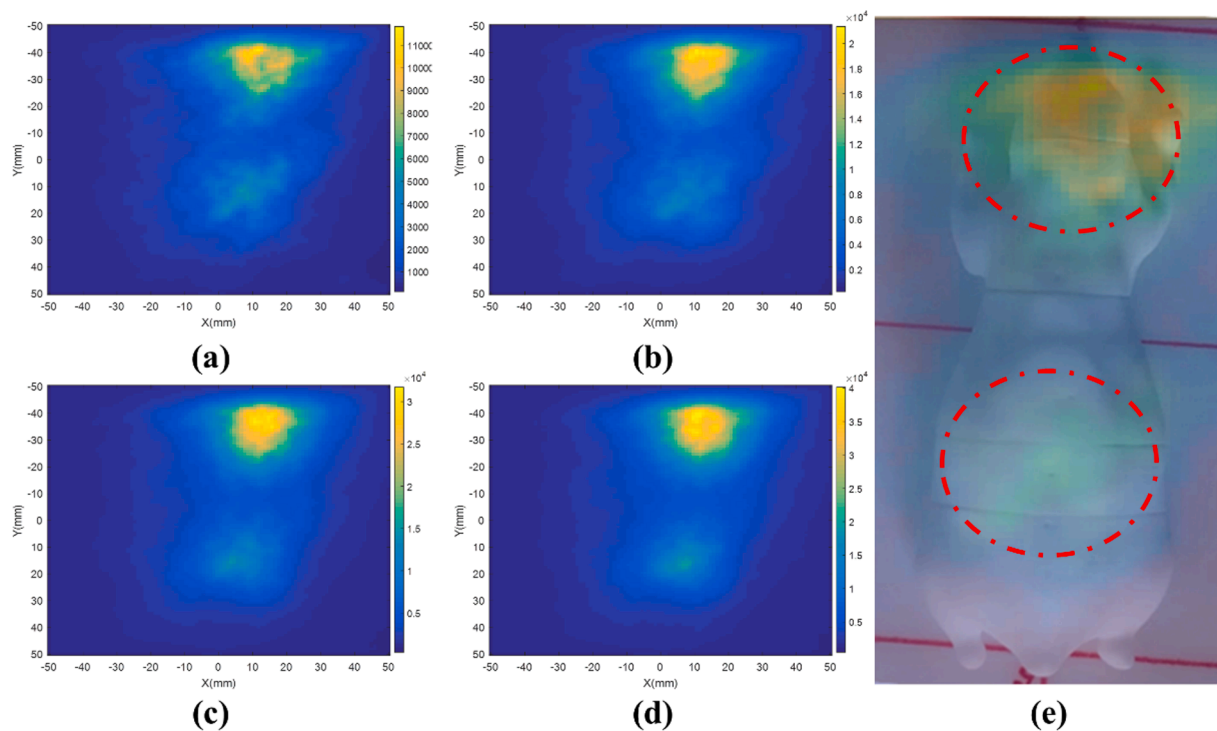
Fig. 11. Reconstruction results at different detection times. (a–d) Reconstruction results of ordered OE-RR algorithm under detection times of 15, 30, 45, and 60 min. (e) Result of 15 min detection superimposed with the mouse phantom.

4. Discussion

In this study, the performance of the 3D-CZT CC in radiopharmaceutical imaging is analyzed. The imaging process is simulated using the Monte Carlo methods. As a result of the excellent energy resolution of the 3D-CZT CC, the measured Compton scattering angles are not obviously influenced. However, the calculated Compton axis will be heavily influenced by the spatial resolution.

To reduce these influences, we analyze the relation between the Compton axis deviation and the distance of the Compton and photoelectronic interactions. By increasing $D_{scatter\_absorb}$ to over 10 mm, the phi angle deviation is reduced from ~50% to ~5%, and the theta angle deviation is reduced from ~200% to ~20%. These results are similar to those of other studies [33]. However, as the $D_{scatter\_absorb}$ increases, the count of effective Compton events decreases exponentially. In simulations, there are 215,171 effective Compton events without event distance selection. When the $D_{scatter\_absorb}$ is more than 5 mm, 10 mm, and 15 mm, the counts of effective Compton events decreased to 67343, 18,400 and 3848, respectively. Therefore, it is necessary to balance the count of effective Compton events with the error caused by pixelation effect. To ensure the considerable count of effective Compton events for reconstruction, we set the minimum distance between the Compton and photoelectronic interactions to be 10 mm for selecting the effective Compton events. Comparing the results with different reconstruction algorithms reveals that there are some artifacts in the reconstruction results of the SBP and OE algorithms with the incorrected projection data. Using the ordered OE-RR algorithm, the artifacts in the reconstruction result are significantly reduced, and the quality of the reconstructed results is significantly improved. This trend is similar to that in previous studies on proton range verification [27]. Quantitative analysis shows that using order OE-RR algorithm, the value of V_{con} can be increased by about 7.56 times compared with SBP and 1.40 times compared with OE algorithm. It can also be seen from the reconstructed radiopharmaceutical distribution that the SBP result has a high count in the background and the radiopharmaceutical position will shift from the real position. Without resolution recovery, order OE algorithm can significantly reduce the artifacts in the background, but the fluctuation of the image is significantly enhanced for the low activity area. Therefore, for low activity areas, the effect of image quality improvement caused by resolution recovery may be more obvious.

For experimental data, the event selection method and resolution recovery method are also applicable. When using events with higher $D_{scatter\_absorb}$ for reconstructing, the results obtained by either SBP or order OE-RR algorithm will be significantly improved. The artifacts in results reconstructed by order OE-RR are significantly less than those in SBP. However, the image quality reconstructed by experimental data are worse than that by simulation data. Many factors will affect the experimental results, but they are difficult to be taken into account in simulations, such as electronic noise, the influence of neighboring pixels et al. In the simulations, the energy resolution is obtained by fitting the measured data, which would take into account the influence of electronic noise, Doppler broadening and other factors to a certain extent. Moreover, the methods used to determine the type of reaction event in simulations and experiments are different. The scattering and absorption events in the simulated data are absolutely true, but for experiment data, the event types of the two anode signals output by the detector should be judged according to energy deposition. For gamma rays with 511 keV which occurs Compton scattering reaction in CZT, the probability that the energy of scattered gamma ray is greater than that of scattered electron is only about 58.34%, which is similar to the results of other studies [32]. Therefore, almost 40% of the effective Compton events used for reconstructing may have an error in the event type, thus deteriorating the imaging quality. In the follow-up experimental research, more effective methods need to be adopted to improve the reconstructed image quality, for example using machine-learning approach to distinguish the Compton events from the background or using neural network method to judge the event type [34–36]. Finally, the detection performance of the image device under different measurement times is analyzed. With the increase of the detection time, the quality of the reconstruction results is gradually optimized. Based on the experimental conditions set in this study, the count rate of effective Compton events after event selecting can reach about 14,697 per hour,

and the reconstruction time of one event is about 2.45 ± 0.28 ms with the Intel Xeon(R) CPU E5-2699 v4. Within 15 min detection time, the quality of the reconstruction results can be comparable to those of some published studies using different imaging devices [17,37]. This result provides a basis for the radiopharmaceutical imaging application of the 3D-CZT image device.

At present, this work demonstrates the feasibility of using a 3D-CZT CC for radiopharmaceutical distribution imaging at the level of clinical activity, but there are still some problems that need to be further studied. In the follow-up, it is also necessary to carry out researches regarding the detection device improvement and reconstruction algorithm optimization. Of course, animal studies for further demonstrating the spatial resolution and practical efficiency will be helpful for further development of the methodology. Multi-angle measurement could be carried to realize the 3D reconstruction of radiopharmaceutical distribution, and the results of CC based on multi-angle measurement should be compared with PET or SPECT results to further analyze the feasibility and value of this method in practical clinical practice.

5. Conclusion

In this study, we propose the use of the single-layer 3D-CZT CC for radiopharmaceutical imaging. The event selection method based on event distance is proposed to reduce the deviation of the calculated Compton scattering angle and Compton axis. The ordered OE-RR is used to eliminate artifacts in the reconstruction results. The experimental results show that the imaging device can obtain an accurate radiopharmaceutical distribution within the detection time of 15 min and the reconstruction time is about 10 s, which shows the promising application of the proposed methodology.

Acknowledgments

References

[1] Filippou V, Tsoumpas C. Recent advances on the development of phantoms using 3D printing for imaging with CT, MRI, PET, SPECT, and ultrasound. Med Phys 2018;45:740–60. https://doi.org/10.1002/mp.13058.

[2] Russo P, Di Lillo F, Corvino V, Frallicciardi PM, Sarno A, Mettivier G. CdTe compact gamma camera for coded aperture imaging in radioguided surgery. Phys Medica 2020;69:223–32. https://doi.org/10.1016/j.ejmp.2019.12.024.

[3] Geng C, Ai Y, Tang X, Shu D, Gong C, Du M, et al. Quantum dots enhanced Cerenkov luminescence imaging. Nucl Sci Tech 2019;30:1–5. https://doi.org/10.1007/s41365-019-0599-x.

[4] Del Guerra A, Belcari N. State-of-the-art of PET, SPECT and CT for small animal imaging. Nucl Instrum Meth A 2007;583:119–24. https://doi.org/10.1016/j.nima.2007.08.187.

[5] Kishimoto A, Kataoka J, Koide A, Sueoka K, Iwamoto Y, Taya T, et al. Development of a compact scintillator-based high-resolution Compton camera for molecular imaging. Nucl Instrum Meth A 2017;845:656–9.

[6] Motomura S, Kanayama Y, Haba H, Watanabe Y, Enomoto S. Multiple molecular simultaneous imaging in a live mouse using semiconductor Compton camera. J Anal Atom Spectrom 2008;23:1089–92. https://doi.org/10.1039/B802964D.

[7] Tian F, Geng C-R, Tang X-B, Shu D-Y, Ye H-F, Bortolussi S, et al. Analysis of influencing factors on the method for determining boron concentration and dose through dual prompt gamma detection. Nucl Sci Tech 2021;32(4). https://doi.org/10.1007/s41365-021-00873-3.

[8] Fontana M, Dauvergne D, Létang JM, Ley J-L, Testa É. Compton camera study for high efficiency SPECT and benchmark with Anger system. Phys Med Biol 2017;62:8794. https://doi.org/10.1088/1361-6560/aa926a.

[9] Amato E, Auditore L, Campennì A, Minutoli F, Cucinotta M, Sindoni A, et al. A didactic experiment showing the Compton scattering by means of a clinical gamma camera. Phys Medica 2017;38:119–21.

[10] Kabuki S, Hattori K, Kohara R, Kunieda E, Kubo A, Kubo H, et al. Development of electron tracking Compton camera using micro pixel gas chamber for medical imaging. Nucl Instrum Meth A 2007;580(2):1031–5.

[11] Roellinghoff F, Richard M-H, Chevallier M, Constanzo J, Dauvergne D, Freud N, et al. Design of a Compton camera for 3D prompt-γ imaging during ion beam therapy. Nucl Instrum Meth A 2011;648:S20–3. https://doi.org/10.1016/j.nima.2011.01.069.

[12] Gong C-H, Tang X-B, Shu D-Y, Yu H-Y, Geng C-R. Optimization of the Compton camera for measuring prompt gamma rays in boron neutron capture therapy. Appl Radiat Isot 2017;124:62–7.

[13] Watanabe S, Tanaka T, Nakazawa K, Mitani T, Oonuki K, Takahashi T, et al. A Si/CdTe semiconductor compton camera. IEEE T Nucl Sci 2005;52(5):2045–51.

[14] Kataoka J, Kishimoto A, Nishiyama T, Fujita T, Takeuchi K, Kato T, et al. Handy Compton camera using 3D position-sensitive scintillators coupled with large-area monolithic MPPC arrays. Nucl Instrum Meth A 2013;732:403–7.

[15] Turecek D, Jakubek J, Trojanova E, Sefc L. Single layer Compton camera based on Timepix3 technology. J Instrum 2020;15:C01014. https://doi.org/10.1088/1748-0221/15/01/C01014.

[16] Liprandi S, Mayerhofer M, Aldawood S, Binder T, Dedes G, Miani A, et al. Sub-3mm spatial resolution from a large monolithic LaBr 3 (Ce) scintillator. CDBME 2017;3 (2):655–9.

[17] Sakai M, Yamaguchi M, Nagao Y, Kawachi N, Kikuchi M, Torikai K, et al. In vivo simultaneous imaging with 99mTc and 18F using a Compton camera. Phys Med Biol 2018;63:205006. 10.1088/1361-6560/aae1d1.

[18] Golnik C, Bemmerer D, Enghardt W, Fiedler F, Hueso-González F, Pausch G, et al. Tests of a Compton imaging prototype in a monoenergetic 4.44 MeV photon field—a benchmark setup for prompt gamma-ray imaging devices. J Instrum 2016; 11:P06009. 10.1088/1748-0221/11/06/P06009.

[19] He Z, Li W, Knoll GF, Wehe DK, Berry J, Stahle CM. 3-D position sensitive CdZnTe gamma-ray spectrometers. Nucl Instrum Meth A 1999;422:173–8. https://doi.org/10.1016/S0168-9002(98)00950-4.

[20] Feng Z, Zhong H, Dan X. Analysis of detector response using 3-D position-sensitive CZT gamma-ray spectrometers. IEEE T Nucl Sci 2005;51:3098–104. https://doi.org/10.1109/TNS.2004.839078.

[21] Liu Y, Fu J, Li Y, Li Y, Ma X, Zhang L. Preliminary results of a Compton camera based on a single 3D position-sensitive CZT detector. Nucl Sci Tech 2018;29:1–11. https://doi.org/10.1007/s41365-018-0483-0.

[22] Shy D, Xia J, He Z. Artifacts in high-energy Compton imaging with 3-D position-sensitive CdZnTe. IEEE T Nucl Sci 2020;67:1920–8. https://doi.org/10.1109/TNS.2020.3005834.

[23] Draeger E, Mackin D, Peterson S, Chen H, Avery S, Beddar S, et al. 3D prompt gamma imaging for proton beam range verification. Phys Med Biol 2018;63: 035019. https://doi.org/10.1088/1361-6560/aaa203.

[24] Peterson SW, Robertson D, Polf J. Optimizing a three-stage Compton camera for measuring prompt gamma rays emitted during proton radiotherapy. Phys Med Biol 2010;55:6841–56. https://doi.org/10.1088/0031-9155/55/22/015.

[25] Sitek A. Reconstruction of emission tomography data using origin ensembles. IEEE T Med Imaging 2010;30:946–56. https://doi.org/10.1109/TMI.2010.2098036.

[26] Andreyev A, Celler A, Ozsahin I, Sitek A. Resolution recovery for Compton camera using origin ensemble algorithm. Med Phys 2016;43:4866–76. https://doi.org/10.1118/1.4959551.

[27] Yao Z, Xiao Y, Chen Z, Wang B, Hou Q. Compton-based prompt gamma imaging using ordered origin ensemble algorithm with resolution recovery in proton therapy. Sci Rep-UK 2019;9:1–15. https://doi.org/10.1038/s41598-018-37623-2.

[28] Geronimo GD, Vernon E, Ackley K, Dragone A, Fried J, Connor PO, et al. Readout ASIC for 3D position-sensitive detectors. IEEE Nuclear Science Symposium Conference Record 2007;2007:32–41. https://doi.org/10.1109/NSSMIC.2007.4436284.

[29] De Geronimo G, Vernon E, Ackley K, Dragone A, Fried J, O'Connor P, et al. Readout ASIC for 3D position-sensitive detectors. IEEE T Nucl Sci 2008;55(3): 1593–603.

[30] Dogdas B, Stout D, Chatziioannou AF, Leahy RM. Digimouse: a 3D whole body mouse atlas from CT and cryosection data. Phys Med Biol 2007;52(3):577–87.

[31] Ordonez CE, Chang W, Bolozdynya A. Angular uncertainties due to geometry and spatial resolution in Compton cameras. IEEE T Nucl Sci 1999;3:1142–7. https://doi.org/10.1109/23.790848.

[32] Kim Y, Lee T, Lee W. Radiation measurement and imaging using 3D position sensitive pixelated CZT detector. Nucl Eng Technol 2019;51:1417–27. https://doi.org/10.1016/j.net.2019.03.009.

[33] Cui J, Chinn G, Levin CS. Fast and accurate 3D Compton cone projections on GPU using CUDA. IEEE Nuclear Science Symposium Conference Record: IEEE 2011; 2011:2572–5. https://doi.org/10.1109/NSSMIC.2011.6152694.

[34] Muñoz E, Ros A, Borja-Lloret M, Barrio J, Dendooven P, Oliver JF, et al. Proton range verification with MACACO II Compton camera enhanced by a neural network for event selection. Sci Rep-UK 2021;11(1). https://doi.org/10.1038/s41598-021-88812-5.

[35] Ohno M, Fukazawa Y, Mizuno T, Takahashi H, Tanaka Y, Ji K, et al. Event-selection technique for the multi-layer Si− CdTe Compton camera onboard Hitomi. Nucl Instrum Meth A 2019;924:327–31. https://doi.org/10.1016/j.nima.2018.09.114.

[36] Zoglauer A, Boggs SE. Application of neural networks to the identification of the compton interaction sequence in compton imagers. IEEE Nuclear Science Symposium Conference Record: IEEE 2007;2007:4436–41. https://doi.org/10.1109/NSSMIC.2007.4437096.

[37] Kabuki S, Kimura H, Amano H, Nakamoto Y, Tanimori T. Electron-tracking Compton gamma-ray camera for small animal and phantom imaging. Nucl Instrum Meth A 2010;251:606–7. https://doi.org/10.1016/j.nima.2010.03.085.